K. Stein
Department of Physics,
Bethel College,
St. Paul, MN 55112

T. Tezduyar

V. Kumar

S. Sathe

Mechanical Engineering,
Rice University,
MS 321,
Houston, TX 77005

R. Benney
Natick Soldier Center,
Natick, MA 01760

E. Thornburg

C. Kyle

U.S. Military Academy,
West Point, NY 10996

T. Nonoshita
Nepon, Inc.,
Kanagawa, Japan

Aerodynamic Interactions Between Parachute Canopies

Aerodynamic interactions between parachute canopies can occur when two separate parachutes come close to each other or in a cluster of parachutes. For the case of two separate parachutes, our computational study focuses on the effect of the separation distance on the aerodynamic interactions, and also focuses on the fluid-structure interactions with given initial relative positions. For the aerodynamic interactions between the canopies of a cluster of parachutes, we focus on the effect of varying the number and arrangement of the canopies. [DOI: 10.1115/1.1530634]

1 Introduction

The performance of a parachute might be influenced by the aerodynamic and fluid-structure interactions of its canopy with other parachute canopies. In this paper, we describe our computational model for such interactions, and present numerical results from simulations for two different types of interactions. In the first case, our investigation focuses on the aerodynamic and fluid-structure interactions between the canopies of two separate parachutes coming close to each other. We study how the aerodynamic interactions depend on the horizontal distance between the parachutes. We also study how such interactions are influenced when our computational model includes the fluid-structure interactions (FSI) between the parachute canopy and the surrounding flow field. For this, we start with given initial relative positions. In the second case, we investigate the aerodynamic interactions between the canopies of a cluster of parachutes. We simulate the interactions for clusters with three, four, five, and six canopies, and investigate how such interactions depend on the number of canopies as well as the spatial arrangement of these canopies.

These simulations, in addition to providing some initial results for the aerodynamic and fluid-structure interactions between parachute canopies, show how the computational methods described can be used for parachute applications. The interaction between the parachute canopy and the surrounding flow field is an essential component of a realistic parachute simulation, and thus the ability to predict parachute FSI is recognized as an important challenge within the parachute research community, [1–5]. In our follow-on studies, we plan to take more extensively into account the complex FSI involved at various stages of parachute systems, from initial deployment to landing.

For the cases simulated in this paper, the parachutes are operating at sufficiently low speeds, and, therefore, the aerodynamics is governed by the Navier-Stokes equations of incompressible flows. For the problems where we limit our attention to the aerodynamic interaction between the parachute canopies, the canopies are not experiencing any shape changes or relative motions. Therefore, in those simulations, the fluid dynamics computations are based on a stabilized semi-discrete finite element formulation, [6]. For the cases that involve fluid-structure interactions, on the other hand, the canopies undergo shape changes. In such cases, because the spatial domain occupied by the fluid is varying (i.e., deforming) with respect to time, we use the Deforming-Spatial-Domain/Stabilized Space-Time (DSD/SST) formulation, [6–8], which was developed for flow problems with moving boundaries and interfaces. Both the semi-discrete and space-time methods have been implemented for parallel computing, and the results presented here are from simulations carried out on a CRAY T3E-1200 supercomputer.

2 Computational Model

2.1 Fluid Dynamics. Let $\Omega_t \subset \mathbb{R}^{n_{sd}}$ be the spatial fluid mechanics domain with boundary Γ_t at time $t \in (0,T)$, where the

Contributed by the Applied Mechanics Division of THE AMERICAN SOCIETY OF MECHANICAL ENGINEERS for publication in the ASME JOURNAL OF APPLIED MECHANICS. Manuscript received by the ASME Applied Mechanics Division, Aug. 23, 2001; final revision, Mar. 18, 2002. Associate Editor: W. T. Wheeler. Discussion on the paper should be addressed to the Editor, Prof. Robert M. McMeeking, Department of Mechanical and Environmental Engineering University of California–Santa Barbara, Santa Barbara, CA 93106-5070, and will be accepted until four months after final publication of the paper itself in the ASME JOURNAL OF APPLIED MECHANICS.

subscript t indicates the time-dependence of the spatial domain and its boundary. The Navier-Stokes equations of incompressible flows can be written on Ω_t and $\forall t \in (0,T)$ as

$$\rho\left(\frac{\partial \mathbf{u}}{\partial t}+\mathbf{u}\cdot\nabla\mathbf{u}-\mathbf{f}\right)-\nabla\cdot\boldsymbol{\sigma}=0, \tag{1}$$

$$\nabla\cdot\mathbf{u}=0, \tag{2}$$

where ρ, $\mathbf{u}$, and $\mathbf{f}$ are the density, velocity, and the external force, respectively. The stress tensor $\boldsymbol{\sigma}$ is defined as

$$\boldsymbol{\sigma}(p,\mathbf{u})=-p\mathbf{I}+2\mu\boldsymbol{\varepsilon}(\mathbf{u}). \tag{3}$$

Here p, $\mathbf{I}$, and μ are the pressure, identity tensor, and the viscosity, respectively. The strain rate tensor is defined as

$$\boldsymbol{\varepsilon}(\mathbf{u})=\frac{1}{2}((\nabla\mathbf{u})+(\nabla\mathbf{u})^T). \tag{4}$$

Both Dirichlet and Neumann-type boundary conditions are accounted for:

$$\mathbf{u}=\mathbf{g} \text{ on } (\Gamma_t)_g, \quad \mathbf{n}\cdot\boldsymbol{\sigma}=\mathbf{h} \text{ on } (\Gamma_t)_h. \tag{5}$$

Here $(\Gamma_t)_g$ and $(\Gamma_t)_h$ are complementary subsets of the boundary Γ_t, $\mathbf{n}$ is the unit normal vector at the boundary, and $\mathbf{g}$ and $\mathbf{h}$ are given functions. A divergence-free velocity field is specified as the initial condition.

2.2 Structural Dynamics. Let $\Omega_t^s \subset \mathbb{R}^{n_{xd}}$ be the spatial domain bounded by Γ_t^s, where $n_{xd}=2$ for membranes and $n_{xd}=1$ for cables. The boundary Γ_t^s is composed of $(\Gamma_t^s)_g$ and $(\Gamma_t^s)_h$. Here, the superscript "s" corresponds to the structure. The equations of motion for the structural system are

$$\rho^s\left(\frac{d^2\mathbf{y}}{dt^2}+\eta\frac{d\mathbf{y}}{dt}-\mathbf{f}^s\right)-\nabla\cdot\boldsymbol{\sigma}^s=\mathbf{0}, \tag{6}$$

where $\mathbf{y}$ is the displacement, ρ^s is the material density, $\mathbf{f}^s$ are the external body forces, $\boldsymbol{\sigma}^s$ is the Cauchy stress tensor, and η is the mass-proportional damping coefficient. The damping provides additional stability and is used for problems where time accuracy is not important.

We use a total Lagrangian formulation of the problem. Thus, stresses are expressed in terms of the second Piola-Kirchoff stress tensor $\mathbf{S}$, which is related to the Cauchy stress tensor through a kinematic transformation. Under the assumption of large displacements and rotations, small strains, and no material damping, the membranes and cables are treated as Hookean materials with linear elastic properties. For membranes, under the assumption of plane stress, $\mathbf{S}$ becomes

$$S^{ij}=(\overline{\lambda}_m G^{ij}G^{kl}+\mu_m[G^{il}G^{jk}+G^{ik}G^{jl}])E_{kl}, \tag{7}$$

where for the case of isotropic plane stress

$$\overline{\lambda}_m=\frac{2\lambda_m\mu_m}{(\lambda_m+2\mu_m)}. \tag{8}$$

Here, E_{kl} are the components of the Cauchy-Green strain tensor, G^{ij} are the components of the contravariant metric tensor in the original configuration, and λ_m and μ_m are Lamé constants. For cables, under the assumption of uniaxial tension, $\mathbf{S}$ becomes

$$S^{11}=E_c G^{11}G^{11}E_{11}, \tag{9}$$

where E_c is the cable Young's modulus. To account for stiffness-proportional material damping, the Hookean stress-strain relationships defined by Eqs. (7) and (9) are modified, and E_{kl} is replaced by $\hat{E}_{kl}$, where

$$\hat{E}_{kl}=E_{kl}+\zeta\dot{E}_{kl}. \tag{10}$$

Here, ζ is the stiffness proportional damping coefficient and $\dot{E}_{kl}$ is the time derivative of E_{kl}.

2.3 Semi-Discrete Formulation of Fluid Dynamics. Let us consider a fixed spatial domain Ω and its boundary Γ, where subscript t is dropped from both Ω_t and Γ_t. The domain Ω is discretized into subdomains Ω^e, $e=1,2,\cdots,n_{el}$, where n_{el} is the number of elements. For this discretization, the finite element trial function spaces $\mathcal{S}_u^h$ for velocity and $\mathcal{S}_p^h$ for pressure, and the corresponding test function spaces $\mathcal{V}_u^h$ and $\mathcal{V}_p^h$ are defined as follows:

$$\mathcal{S}_u^h=\{\mathbf{u}^h|\mathbf{u}^h\in[H^{1h}(\Omega)]^{n_{sd}},\mathbf{u}^h\doteq\mathbf{g}^h \text{ on } \Gamma_g\}, \tag{11}$$

$$\mathcal{V}_u^h=\{\mathbf{w}^h|\mathbf{w}^h\in[H^{1h}(\Omega)]^{n_{sd}},\mathbf{w}^h\doteq\mathbf{0} \text{ on } \Gamma_g\}, \tag{12}$$

$$\mathcal{S}_p^h=\mathcal{V}_p^h=\{q^h|q^h\in H^{1h}(\Omega)\}. \tag{13}$$

Here $H^{1h}(\Omega)$ is the finite-dimensional function space over Ω. The stabilized formulation is written as follows: Find $\mathbf{u}^h\in\mathcal{S}_\mathbf{u}^h$ and $p^h\in\mathcal{S}_p^h$ such that $\forall\mathbf{w}^h\in\mathcal{V}_\mathbf{u}^h$ and $q^h\in\mathcal{V}_p^h$:

$$\begin{aligned}
&\int_\Omega \mathbf{w}^h\cdot\rho\left(\frac{\partial\mathbf{u}^h}{\partial t}+\mathbf{u}^h\cdot\nabla\mathbf{u}^h-\mathbf{f}^h\right)d\Omega\\
&\quad+\int_\Omega \boldsymbol{\varepsilon}(\mathbf{w}^h):\boldsymbol{\sigma}(p^h,\mathbf{u}^h)d\Omega-\int_{\Gamma_h}\mathbf{w}^h\cdot\mathbf{h}^h d\Gamma\\
&\quad+\int_\Omega q^h\nabla\cdot\mathbf{u}^h d\Omega\\
&\quad+\sum_{e=1}^{n_{el}}\int_{\Omega^e}\frac{1}{\rho}[\tau_{\mathrm{SUPG}}\rho\mathbf{u}^h\cdot\nabla\mathbf{w}^h+\tau_{\mathrm{PSPG}}\nabla q^h]\\
&\quad\times[\mathbf{Ł}(p^h,\mathbf{u}^h)-\rho\mathbf{f}^h]d\Omega\\
&\quad+\sum_{e=1}^{n_{el}}\int_{\Omega^e}\tau_{\mathrm{LSIC}}\nabla\cdot\mathbf{w}^h\rho\nabla\cdot\mathbf{u}^h d\Omega=0,
\end{aligned} \tag{14}$$

where

$$\mathbf{Ł}(q^h,\mathbf{w}^h)=\rho\left(\frac{\partial\mathbf{w}^h}{\partial t}+\mathbf{u}^h\cdot\nabla\mathbf{w}^h\right)-\nabla\cdot\boldsymbol{\sigma}(q^h,\mathbf{w}^h). \tag{15}$$

In this formulation, τ_{SUPG}, τ_{PSPG}, and τ_{LSIC} are the stabilization parameters, [6,9].

2.4 DSD/SST Formulation of Fluid Dynamics. In discretization of the space-time domain, the time interval $(0,T)$ is partitioned into subintervals $I_n=(t_n,t_{n+1})$, where t_n and t_{n+1} belong to an ordered series of time levels $0=t_0<t_1\cdots<t_N=T$. Let $\Omega_n=\Omega_{t_n}$ and $\Gamma_n=\Gamma_{t_n}$ to simplify the notation. The space-time slab Q_n is defined as the domain enclosed by the surfaces Ω_n, Ω_{n+1}, and P_n, where P_n is the lateral surface of Q_n described by the boundary Γ_n as t traverses I_n.

The Dirichlet and Neumann-type boundary conditions are specified over $(P_n)_g$ and $(P_n)_h$. For this discretization, the finite element trial function spaces $(\mathcal{S}_\mathbf{u}^h)_n$ for velocity and $(\mathcal{S}_p^h)_n$ for pressure, and the corresponding test function spaces $(\mathcal{V}_\mathbf{u}^h)_n$ and $(\mathcal{V}_p^h)_n$ are defined as follows:

$$(\mathcal{S}_\mathbf{u}^h)_n=\{\mathbf{u}^h|\mathbf{u}^h\in[H^{1h}(Q_n)]^{n_{sd}},\mathbf{u}^h\doteq\mathbf{g}^h \text{ on } (P_n)_g\}, \tag{16}$$

$$(\mathcal{V}_\mathbf{u}^h)_n=\{\mathbf{w}^h|\mathbf{w}^h\in[H^{1h}(Q_n)]^{n_{sd}},\mathbf{w}^h\doteq\mathbf{0} \text{ on } (P_n)_g\}, \tag{17}$$

$$(\mathcal{S}_p^h)_n=(\mathcal{V}_p^h)_n=\{q^h|q^h\in H^{1h}(Q_n)\}. \tag{18}$$

Here $H^{1h}(Q_n)$ is the finite-dimensional function space over the space-time slab Q_n. Over the element domain, this space is formed by using first-order polynomials in both space and time. The interpolation functions are continuous in space but discontinuous in time.

The DSD/SST formulation is written as follows: Given $(\mathbf{u}^h)_n^-$, find $\mathbf{u}^h\in(\mathcal{S}_\mathbf{u}^h)_n$ and $p^h\in(\mathcal{S}_p^h)_n$ such that $\forall\mathbf{w}^h\in(\mathcal{V}_\mathbf{u}^h)_n$ and $q^h\in(\mathcal{V}_p^h)_n$:

$$\int_{Q_n} \mathbf{w}^h \cdot \rho \left(\frac{\partial \mathbf{u}^h}{\partial t} + \mathbf{u}^h \cdot \nabla \mathbf{u}^h - \mathbf{f}^h \right) dQ$$
$$+ \int_{Q_n} \boldsymbol{\varepsilon}(\mathbf{w}^h) : \boldsymbol{\sigma}(p^h, \mathbf{u}^h) dQ - \int_{(P_n)_h} \mathbf{w}^h \cdot \mathbf{h}^h dP$$
$$+ \int_{Q_n} q^h \nabla \cdot \mathbf{u}^h dQ$$
$$+ \int_{\Omega_n} (\mathbf{w}^h)_n^+ \cdot \rho((\mathbf{u}^h)_n^+ - (\mathbf{u}^h)_n^-) d\Omega$$
$$+ \sum_{e=1}^{(n_{el})_n} \int_{Q_n^e} \frac{\tau_{\mathrm{LSME}}}{\rho} \mathbf{Ł}(q^h, \mathbf{w}^h) \cdot$$
$$[\mathbf{Ł}(p^h, \mathbf{u}^h) - \rho \mathbf{f}^h] dQ$$
$$+ \sum_{e=1}^{n_{el}} \int_{Q_n^e} \tau_{\mathrm{LSIC}} \nabla \cdot \mathbf{w}^h \rho \nabla \cdot \mathbf{u}^h dQ = 0. \quad (19)$$

This formulation is sequentially applied to all space-time slabs $Q_0, Q_1, Q_2, \ldots, Q_{N-1}$. The computation starts with

$$(\mathbf{u}^h)_0^- = \mathbf{u}_0, \quad \nabla \cdot \mathbf{u}_0 = 0 \quad \text{on} \quad \Omega_0. \quad (20)$$

Here τ_{LSME} is the stabilization parameter (see [9,10]). For an earlier, detailed reference on this formulation see [6].

2.5 Structural Dynamics Formulation. The semi-discrete finite element formulation for the structural dynamics is based on the principle of virtual work:

$$\int_{\Omega_0^s} \rho^s \frac{d^2 \mathbf{y}^h}{dt^2} \cdot \mathbf{w}^h d\Omega^s + \int_{\Omega_0^s} \eta \rho^s \frac{d\mathbf{y}^h}{dt} \cdot \mathbf{w}^h d\Omega^s + \int_{\Omega_0^s} \mathbf{S}^h : \delta \mathbf{E}(\mathbf{w}^h) d\Omega^s$$
$$= \int_{\Omega_t^s} (\mathbf{t} + \rho^s \mathbf{f}^s) \cdot \mathbf{w}^h d\Omega^s. \quad (21)$$

Here the weighting function $\mathbf{w}^h$ is also the virtual displacement. The air pressure force on the canopy surface is represented by vector **t**. The pressure term is a "follower force" (since it "follows" the deforming structural geometry) and thus increases the overall nonlinearity of the formulation. The left-hand-side terms of Eq. (21) are referred to in the original configuration and the right-hand-side terms for the deformed configuration at time t.

Upon discretization using appropriate function spaces, a nonlinear system of equations is obtained at each time-step. In solving that nonlinear system with an iterative method, we use the following incremental form:

$$\left[\frac{\mathbf{M}}{\beta \Delta t^2} + \frac{(1-\alpha)\gamma \mathbf{C}}{\beta \Delta t} + (1-\alpha)\mathbf{K} \right] \Delta \mathbf{d}^i = \mathbf{R}^i, \quad (22)$$

where

$$\mathbf{C} = \eta \mathbf{M} + \zeta \mathbf{K}. \quad (23)$$

Here **M** is the mass matrix, **K** is the consistent tangent matrix associated with the internal elastic forces, **C** is a damping matrix, $\mathbf{R}^i$ is the residual vector at the ith iteration, and $\Delta \mathbf{d}^i$ is the ith increment in the nodal displacements vector **d**. In Eq. (22), all of the terms known from the previous iteration are lumped into the residual vector $\mathbf{R}^i$. The parameters α, β, γ are part of the Hilber-Hughes-Taylor, [11], scheme, which is used here for time-integration.

2.6 Mesh Update Method. How the mesh should be updated depends on several factors, such as the complexity of the moving boundary or interface and overall geometry, how unsteady the moving boundary or interface is, and how the starting mesh was generated. In general, the mesh update could have two components: moving the mesh for as long as it is possible, and full or partial remeshing (i.e., generating a new set of elements, and sometimes also a new set of nodes) when the element distortion becomes too high.

In mesh moving strategies, the only rule the mesh motion needs to follow is that at the moving boundary or interface the normal velocity of the mesh has to match the normal velocity of the fluid. Beyond that, the mesh can be moved in any way desired, with the main objective being to reduce the frequency of remeshing. In three-dimensional simulations, if the remeshing requires calling an automatic mesh generator, the cost of automatic mesh generation becomes a major reason for trying to reduce the frequency of remeshing. Furthermore, when we remesh, we need to project the solution from the old mesh to the new one. This introduces projection errors. Also, in three-dimensional, the computing time consumed by this projection step is not a trivial one. All these factors constitute a strong motivation for designing mesh update strategies which minimize the frequency of remeshing.

In some cases where the changes in the shape of the computational domain allow it, a special-purpose mesh moving method can be used in conjunction with a special-purpose mesh generator. In such cases, simulations can be carried out without calling an automatic mesh generator and without solving any additional equations to determine the motion of the mesh. One of the earliest examples of that, two-dimensional computation of sloshing in a laterally vibrating container, can be found in [6]. Extension of that concept to three-dimensional parallel computation of sloshing in a vertically vibrating container can be found in [12].

In general, however, we use an automatic mesh moving scheme, [13], to move the nodal points, as governed by the equations of linear elasticity, and where the smaller elements enjoy more protection from mesh deformation. The motion of the internal nodes is determined by solving these additional equations, with the boundary conditions for these mesh motion equations specified in such a way that they match the normal velocity of the fluid at the interface. In computation of fluid-structure interactions of parachute systems reported here we use this automatic mesh moving technique.

3 Numerical Examples

For fluid dynamics equations we use tetrahedral meshes. The parachute canopy surface is representative of a C-9 parachute for cases with only aerodynamic interactions, and a T-10 parachute for cases with fluid-structure interactions. In simulation of the aerodynamic interactions between two parachutes, the parachute model consists of the canopy and a paratrooper. For the fluid-structure interactions of two parachutes and for the aerodynamic interactions in clusters of parachutes, we only consider the canopies. Figure 1 shows the parachute canopy surface mesh and and the paratrooper. The simulations are carried out at a Reynolds number (based on the canopy diameter) of approximately 5 million.

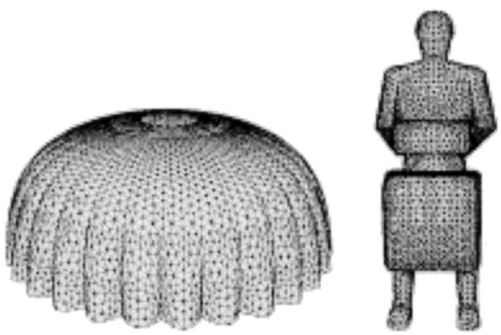

Fig. 1 Aerodynamic interactions of two parachutes. Parachute canopy (left), paratrooper (right).

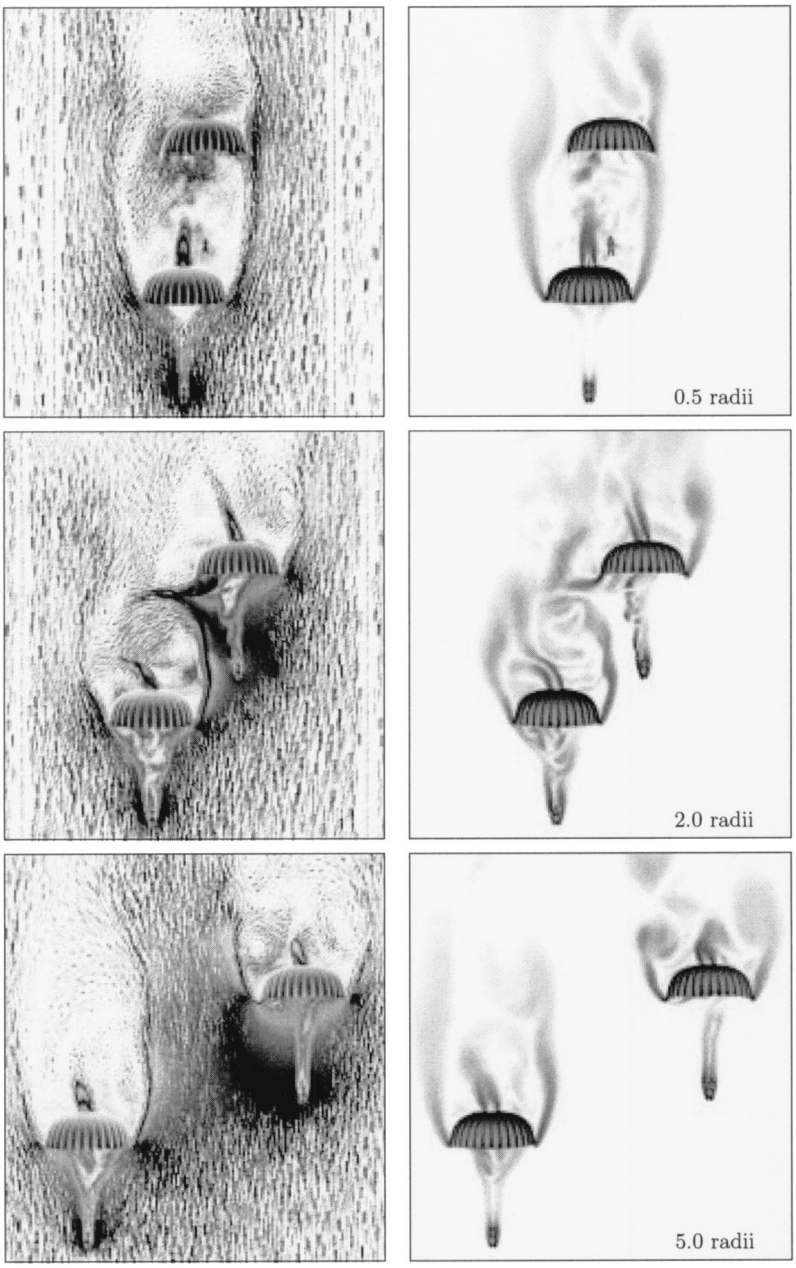

Fig. 2 Aerodynamic interactions of two parachutes. Velocity (left), vorticity (right).

3.1 Aerodynamic Interactions of Two Parachutes. A series of simulations are carried out for the aerodynamic interactions between two separate parachutes, where each parachute consists of a round canopy and a paratrooper. The horizontal spacings, defined to be along the x-axis, range from zero to five (inflated) parachute radii. Vertical spacings are held constant at approximately 3.3 feet between the apex of the lower canopy and the feet of the paratrooper. The parachute model is representative of a 28-foot diameter and 28-gore C-9 personnel parachute. Representation of the canopy geometry comes from a separate structural dynamics simulation with a prescribed pressure distribution. Surface representations for the paratrooper and other boundaries in the fluid dynamics model are obtained using a variety of in-house modeling tools. Separate unstructured volume meshes are generated for each case studied. For each of the examples, the two paratrooper and canopy systems are identical, with 8288 triangular faces describing both the upper and lower canopy surfaces, and 11,714 triangular faces representing the paratrooper. The size of the volume meshes varies from case to case. For the case with horizontal spacing of 0.5 radii, we have approximately 1.8 million elements and 300,000 nodes, resulting in approximately 1.2 million coupled equations. In each of the meshes, the mesh refinement is controlled around the paratroopers and canopies and in the wake and interaction regions, so that we have a larger concentration of elements in these regions. Descent velocities of 22 ft/s are represented by imposing a uniform upstream boundary condition at the lower boundary. Other boundary conditions are, no-slip conditions on the paratrooper and canopy surfaces, zero normal velocity and zero shear stress conditions at the side boundaries, and traction-free conditions at the outflow boundary.

The simulations show a strong, adverse interaction between the upper and lower parachutes for spacings of 1.0 radius and less. In these cases, the upper canopy ''loses its wind,'' and experiences negative drag for spacings of 0.5 radii and less. This indicates a

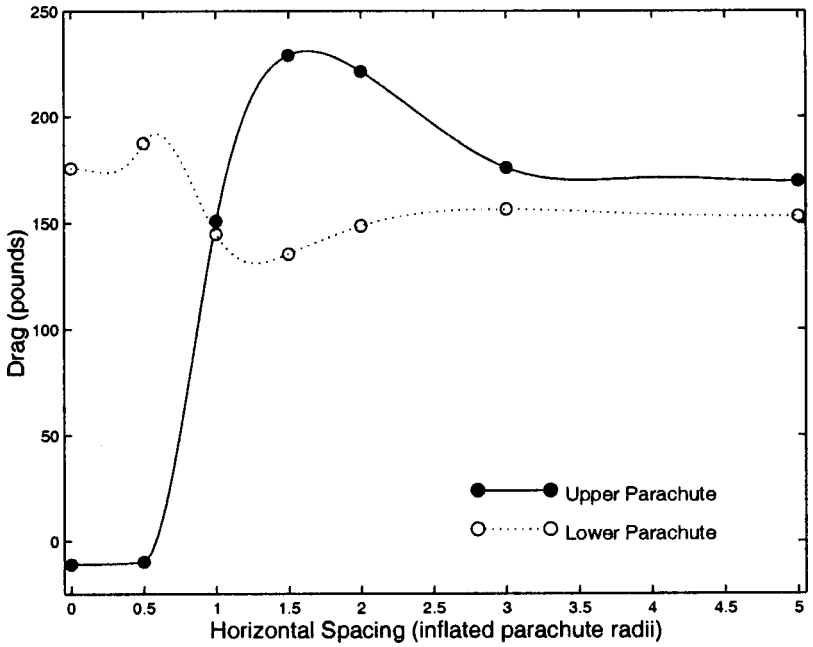

Fig. 3 Aerodynamic interactions of two parachutes. Influence of horizontal spacing on drag, D.

potential for parachute collapse. The flow fields for horizontal spacings of 0.5, 2.0, and 5.0 radii are shown in Fig. 2, with the velocity vectors on the left and the vorticity on the right. For horizontal spacing of 0.5 radii, we clearly see that the upper canopy is caught in the wake of the lower one. For horizontal spacing of 5.0 radii, on the other hand, very little interaction is seen between the two parachute flow fields. The 2.0 radii separation case shows a clear interaction between the two parachutes, but without the upper canopy being trapped in the wake of the lower one.

The interaction between the two parachutes for different horizontal spacings is further understood when we look at the aerodynamic forces acting on the individual canopies. Time-averaged force values were obtained for each horizontal spacing over equivalent time periods, and after the flow fields were fully established. Figure 3 shows, for the lower and upper canopies and for spacings ranging from 0.0 to 5.0 radii, the time-averaged drag (D). The forces shown in these figures are scaled from the computed values based on the C-9 physical dimensions, the prescribed descent velocity, and the air density (these scalings differ from the scaling that was initially presented, [14]). For both canopies, the drag values are fitted to a curve using cubic splines and assuming that the curve (a) is symmetric at zero horizontal spacing and (b) approaches a constant value as the horizontal spacing becomes

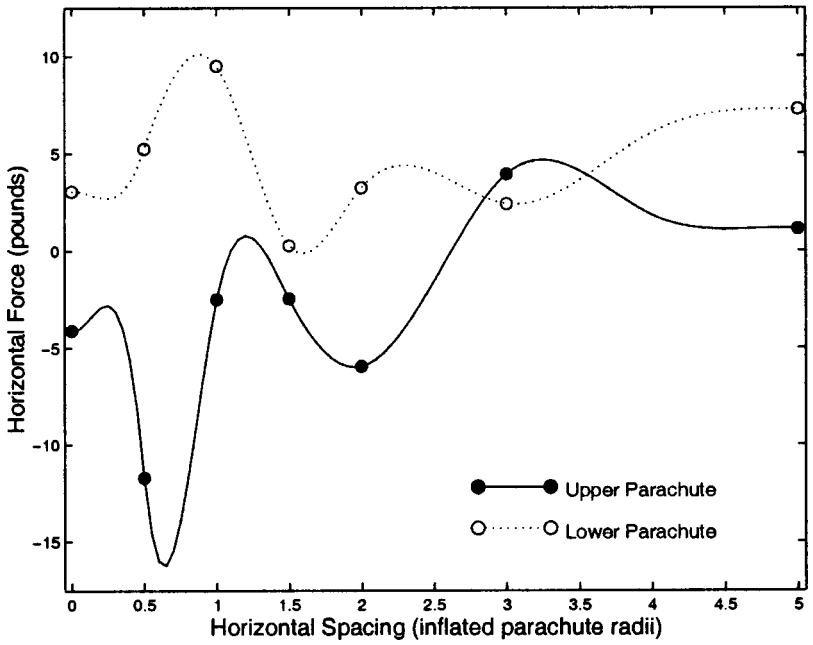

Fig. 4 Aerodynamic interactions of two parachutes. Influence of horizontal spacing on F_x.

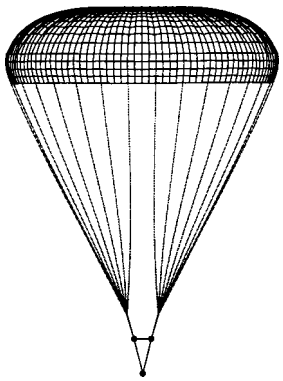

Fig. 5 Fluid-structure interactions of two parachutes. T-10 parachute structural model.

large. At large horizontal spacings, the drag for the lower canopy is expected to approach the same value as the drag for the upper canopy. We see that the drag on the upper parachute can become negative for severe interactions between the parachutes, such as for spacing of 0.5 radii and less. For the 2.0 radii separation case, the drag on the upper canopy remains positive. However, in this case there is a clear interaction between the two parachutes, which could possibly lead to severe structural responses in the fluid-structure interactions of the upper parachute. For the 5.0 radii separation, minimal interaction is seen in the drag history plots, with minor difference in drag for the two parachutes. The proximity of the parachutes to the side and outflow boundaries has some role in the presence of these differences. Extending the boundaries further out and carrying out the computations further in time would make the differences in the time-averaged values of D for the two parachutes even smaller.

Figure 4 shows the time-averaged values of the horizontal force component, F_x. Again, the force histories are fitted to a curve using cubic splines to only show the qualitative trends for the horizontal forces acting on the two parachutes as function of their horizontal separation. For cases with no interaction between the two canopies, the average value of F_x is expected to be zero. The horizontal forces acting on the two canopies are mostly attractive, and are more substantially so for spacings of 2.0 radii and less. For the spacings of 3.0 radii and more, the interaction becomes less evident and the difference between F_x for the upper and lower canopies begins to decrease. The flow field in the wake of each parachute is very unsteady and shows no discernible time-periodic behavior. For these larger spacings, extending the boundaries further out and carrying out the computations further in time would bring the time-averaged values of F_x closer to zero.

3.2 Fluid-Structure Interactions of Two Parachutes. In this simulation, initially the two parachutes have a horizontal spacing of 42 ft, which is approximately 3 (inflated) radii, and a vertical spacing of 56 ft. Here, the parachute model is representative of a standard U.S. Army T-10 personnel parachute. The T-10 is a ''flat extended skirt canopy'' composed of a 35-foot diameter canopy and 30 suspension lines each 29.4 ft long. The canopy is called a ''flat extended skirt canopy'' because in its constructed (or unstressed) configuration it is composed of a main circular section with a circular vent at the apex and an inverted flat ring section, which lies under the main section and is connected to the main section at the outer radius. The lines connect to four risers which attach the payload (or paratrooper). The suspension lines continue as 30 gore-to-gore reinforcements through the parachute canopy and meet at the apex. For the T-10, the vent diameter and the skirt width are both 3.5 ft.

Here the lower canopy is treated as a rigid body, while the upper canopy is allowed to deform due to the response of the parachute structure to the fluid dynamics forces. The structural dynamics model is divided into six distinct material groups; a membrane group, three cable groups, a truss group, and a concentrated mass group. The parachute canopy is composed of 780 biquadratic membrane elements. We have distinct cable groups for the suspension lines, the canopy radial reinforcements, and the risers. The truss and concentrated mass groups define the payload, which has a total weight of 250 pounds. The structure is allowed to fall completely unconstrained.

The parachute canopies are represented as interior surfaces in the fluid mesh (with 17,490 triangular faces on both the upper and

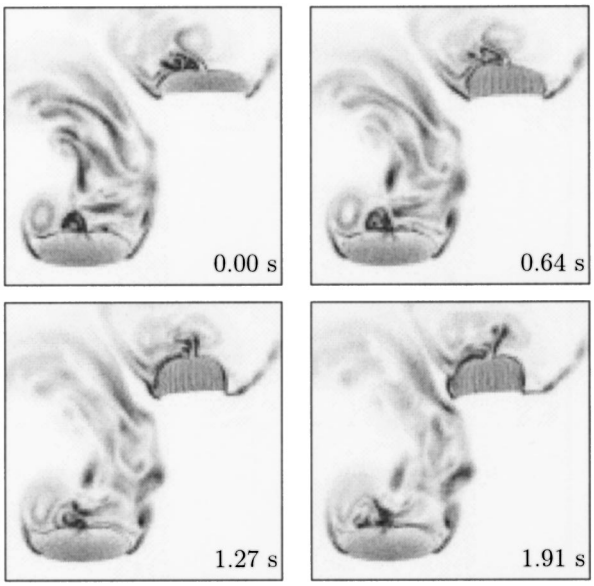

Fig. 6 Fluid-structure interactions of two parachutes. Vorticity at four instants.

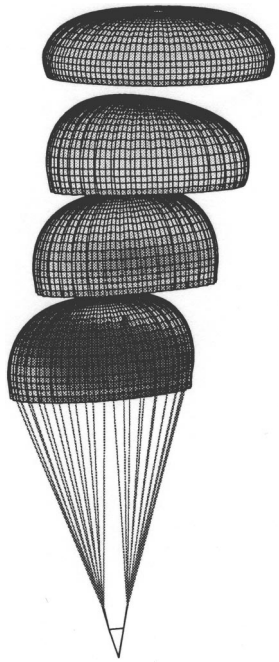

Fig. 7 Fluid-structure interactions of two parachutes. Structural motion and differential pressure distribution at $t=0.00$, 0.64, 1.27, and 1.91 seconds.

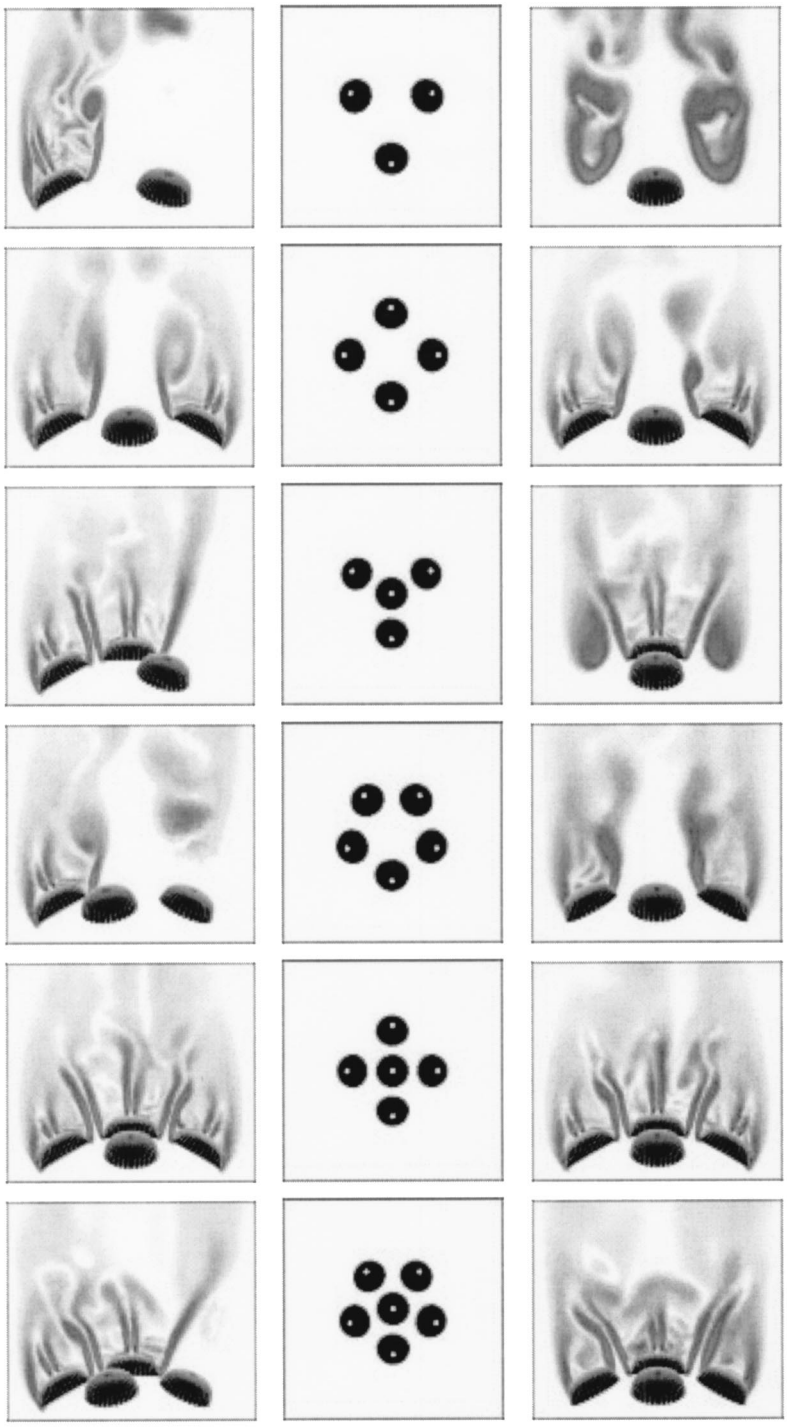

Fig. 8 Aerodynamic interactions in parachute clusters. Vorticity.

lower canopy surfaces). The typical size of the volume mesh is approximately 3.5 million elements and 580 thousand nodes, resulting in approximately 4.6 million coupled equations with the DSD/SST formulation. The automatic mesh update method described earlier is employed to handle the canopy shape changes, with occasional remeshing of the fluid domain. The surface for the upper canopy is assigned a no-slip boundary condition, with velocities coming from the structural dynamics solution. The boundary conditions for the lower canopy and at the outer boundaries are identical to the conditions used in the previous example.

The coupling is achieved iteratively, by transferring the information between the fluid and structure with a least-squares projection. Figure 5 shows the parachute structural model used at the start of the simulation.

Figure 6 shows, at four instants during the simulation, the vorticity field surrounding the two parachutes. The deformation and

motion of the upper canopy is evident. Figure 7 shows, at the same four instants, the structural dynamics of the upper parachute.

3.3 Aerodynamic Interactions in Parachute Clusters. A series of simulations are carried out for the aerodynamic interactions between the canopies in a cluster of parachutes, for three to six canopies. For these simulations, the parachute model is represented by a set of identical C-9 canopies that are positioned and oriented relative to a prescribed confluence point. Two types of configurations are prescribed. First, 3, 4, and 5-canopy clusters are defined with the canopies uniformly distributed at a prescribed angle about the azimuthal axis. Secondly, 4, 5, and 6-canopy clusters are defined with a single canopy in the center and the remaining canopies distributed uniformly at a prescribed angle about the azimuthal axis. The size of the volume mesh varies from case to case. For the 5-canopy cluster with a parachute in the center, we have approximately 2.5 million elements and 450,000 nodes, resulting in approximately 1.9 million coupled equations. Mesh refinement is controlled around the canopies and in the wake and interaction regions. As with the previous example, descent velocities of 22.0 ft/s are represented by imposing a uniform upstream boundary condition at the lower boundary, and no-slip conditions are imposed on the canopy surfaces.

The computed flow fields at the end of the simulations from these preliminary simulations are shown in Fig. 8, with the cluster configurations in the middle column and the corresponding vorticity magnitudes in two cutting planes ($x=0$ and $y=0$) in the left and right columns. These initial simulations qualitatively demonstrate the interactions between the canopies in different cluster arrangements. Further analysis is needed to better understand the other effects influencing the interactions in clusters, such as the preferred arrangements for the canopies, blockage effects due to the finite computational domain, and ultimately the FSI effects. For the examples presented, blockage effects are evident and increase with the number of canopies in the cluster. Experimental studies have been conducted to provide empirical correction factors for blockage effects, [15]. However, these data are dependent on the type of parachute, FSI, and other factors. Further simulations are now being carried out to numerically obtain correction factors for the cases studied.

Additionally, the examples presented neglect the structural response between the canopies in the clusters. The DSD/SST method is now being used to study the dynamics interactions between the canopies in the cluster, treating the individual canopies as rigid bodies. Numerical simulations, [16], have been conducted previously to predict the equilibrium configuration for clusters of three half-scale C-9 parachutes in comparison with experimental data, [17]. In these simulations, equilibrium configurations were determined using a quasi-static approach and imposing a symmetry configuration for the three canopies. The DSD/SST formulation, along with an appropriate mesh-update strategy, allows us to study the interaction of canopies in a cluster in a dynamic fashion. Follow-on simulations will be carried out to predict equilibrium configurations for the 3-canopy cluster with and without an imposed symmetry. Additional simulations will be carried out to study the interactions for the 4, 5, and 6-canopy clusters. Initially, these studies will treat the canopies as rigid bodies, with later simulations including FSI effects.

4 Concluding Remarks

We have described our computational methods for simulation of aerodynamic and fluid-structure interactions between parachute canopies. We considered two different types of problems. In the first case, we focused on the aerodynamic and fluid-structure interactions between the canopies of two separate parachutes in close proximity to one another. We studied the dependence of the aerodynamic interactions on the horizontal distance separating the two parachutes. In this study we observed significant interactions when the horizontal spacing between the parachutes is two canopy radii or less. We also studied how the interactions between the two parachutes are influenced when we include in our computational model the fluid-structure interactions (FSI). The significant amount of structural response we observe in this study for the upper parachute makes it clear that the FSI play a key role in making this class of simulations more realistic. In the second case, we focused on the aerodynamic interactions between the canopies of a cluster of parachutes, and investigated the nature of these interactions for three, four, five, and six canopies. In this study, we were able to see the dependence of these interactions not only on the number of canopies but also on the spatial arrangement of these canopies.

This class of simulations can provide a better understanding of the interactions between parachute canopies and help identify the scenarios under which the interactions are most severe. In the cases of severe interactions, more sophisticated fluid-structure interaction models would be required to accurately represent the response of the parachute structure.

Acknowledgment

The work reported in this paper was partially sponsored by NASA JSC, AFOSR, and by the Natick Soldier Center.

References

[1] Peterson, C. W., Strickland, J. H., and Higuchi, H., 1996, ''The Fluid Dynamics of Parachute Inflation,'' Annu. Rev. Fluid Mech., **28**, pp. 361–387.
[2] Benney, R. J., and Stein, K. R., 1996, ''A Computational Fluid Structure Interaction Model for Parachute Inflation,'' J. Aircr., **33**, pp. 730–736.
[3] Stein, K. R., Benney, R. J., Kalro, V., Johnson, A. A., and Tezduyar, T. E., 1997, ''Parallel Computation of Parachute Fluid-Structure Interactions,'' AIAA Paper No. 97-1505.
[4] Stein, K., Benney, R., Kalro, V., Tezduyar, T., Leonard, J., and Accorsi, M., 1999, ''3-D Computation of Parachute Fluid-Structure Interactions: Performance and Control,'' AIAA Paper No. 99-1714.
[5] Ibos, C., Lacroix, C., Goy, A., and Bordenave, P., 1999, ''Fluid-Structure Simulation of 3D ram Air Parachute With Sinpa Software,'' AIAA Paper No. 99-1713.
[6] Tezduyar, T. E., 1991, ''Stabilized Finite Element Formulations for Incompressible Flow Computations,'' Adv. Appl. Mech., **28**, pp. 1–44.
[7] Tezduyar, T. E., Behr, M., and Liou, J., 1992, ''A New Strategy for Finite Element Computations Involving Moving Boundaries and Interfaces—The Deforming-Spatial-Domain/Space-Time Procedure: I. The Concept and the Preliminary Tests,'' Comput. Methods Appl. Mech. Eng., **94**, pp. 339–351.
[8] Tezduyar, T. E., Behr, M., Mittal, S., and Liou, J., 1992, ''A New Strategy for Finite Element Computations Involving Moving Boundaries and Interfaces—The Deforming-Spatial-Domain/Space-Time Procedure: II. Computation of Free-Surface Flows, Two-Liquid Flows, and Flows With Drifting Cylinders,'' Comput. Methods Appl. Mech. Eng., **94**, pp. 353–371.
[9] Tezduyar, T. E., and Osawa, Y., 1999, ''Methods for parallel computation of complex flow problems,'' Parallel Comput., **25**, pp. 2039–2066.
[10] Behr, M., and Tezduyar, T. E., 1994, ''Finite element solution strategies for large-scale flow simulations,'' Comput. Methods Appl. Mech. Eng., **112**, pp. 3–24.
[11] Hilber, H. M., Hughes, T. J. R., and Taylor, R. L., 1977, ''Improved Numerical Dissipation for Time Integration Algorithms in Structural Dynamics,'' Earthquake Eng. Struct. Dyn., **5**, pp. 283–292.
[12] Tezduyar, T., Aliabadi, S., Behr, M., Johnson, A., and Mittal, S., 1993, ''Parallel Finite-Element Computation of 3D Flows,'' IEEE Computer, **26**, pp. 27–36.
[13] Tezduyar, T. E., Behr, M., Mittal, S., and Johnson, A. A., 1992, ''Computation of Unsteady Incompressible Flows With the Finite Element Methods—Space-Time Formulations, Iterative Strategies and Massively Parallel Implementations,'' *New Methods in Transient Analysis*, P. Smolinski, W. K. Liu, G. Hulbert, and K. Tamma, eds. AMD-Vol.143, ASME, New York, pp. 7–24.
[14] Stein, K., Benney, R., Tezduyar, T., Kumar, V., Thornburg, E., Kyle, C., and Nonoshita, T., 2001, ''Aerodynamic Interaction Between Multiple Parachute Canopies,'' *Proceedings of the First MIT Conference on Computational Fluid and Solid Mechanics*, M.I.T. Press, Cambridge, MA.
[15] Macha, J. M., and Buffington, R. J., 1989, ''Wall-Interference Corrections for Parachutes in a Closed Wind Tunnel,'' AIAA Paper No. 89-0900.
[16] Sahu, J., and Benney, R., 1997, ''Prediction of Terminal Descent Characteristics of Parachute Clusters Using CFD,'' AIAA Paper No. 97-1453.
[17] Lee, C. K., Lanza, J., and Buckley, J., 1996, ''Apparatus and Method for Measuring Angular Positions of Parachute Canopies,'' J. Aircr., **33**, pp. 1197–1199.